An Integrative Structural Biology Analysis of Von Willebrand Factor Binding and Processing by ADAMTS-13 in Solution

Laura del Amo-Maestro [1†], **Amin Sagar** [2†], **Petr Pompach** [3,4], **Theodoros Goulas** [1], **Carsten Scavenius** [5], **Diego S. Ferrero** [6], **Mariana Castrillo-Briceño** [1], **Marta Taulés** [7], **Jan J. Enghild** [5], **Pau Bernadó** [2*] and **F. Xavier Gomis-Rüth** [1*]

1 - *Proteolysis Laboratory, Department of Structural Biology, Molecular Biology Institute of Barcelona (CSIC), Barcelona Science Park, c/Baldiri Reixac, 15-21, 08028 Barcelona, Catalonia, Spain*
2 - *Centre de Biochimie Structurale, INSERM, CNRS and Université de Montpellier, 34090 Montpellier, France*
3 - *Institute of Microbiology of the Czech Academy of Sciences, BIOCEV, Prumyslova 595, 252 50 Vestec, Czechia*
4 - *Institute of Biotechnology of the Czech Academy of Sciences, BIOCEV, Prumyslova 595, 252 50 Vestec, Czechia*
5 - *Department of Molecular Biology and Genetics, Aarhus University, Gustav Wieds Vej 10, 8000 Aarhus C, Denmark*
6 - *Laboratory for Viruses and Large Biological Complexes, Department of Structural Biology, Molecular Biology Institute of Barcelona (CSIC), Barcelona Science Park, c/Baldiri Reixac, 15-21, 08028 Barcelona, Catalonia, Spain*
7 - *Scientific and Technological Centers (CCiTUB), University of Barcelona, Lluís Solé i Sabaris, 1-3, 08028 Barcelona, Catalonia, Spain*

Correspondence to Pau Bernadó and F. Xavier Gomis-Rüth: pau.bernado@cbs.cnrs.fr *(P. Bernadó),* xgrcri@ibmb.csic.es *(F.X. Gomis-Rüth)*
https://doi.org/10.1016/j.jmb.2021.166954
Edited by M. Guss

Abstract

Von Willebrand Factor (vWF), a 300-kDa plasma protein key to homeostasis, is cleaved at a single site by multi-domain metallopeptidase ADAMTS-13. vWF is the only known substrate of this peptidase, which circulates in a latent form and becomes allosterically activated by substrate binding. Herein, we characterised the complex formed by a competent peptidase construct (AD13-MDTCS) comprising metallopeptidase (M), disintegrin-like (D), thrombospondin (T), cysteine-rich (C), and spacer (S) domains, with a 73-residue functionally relevant vWF-peptide, using nine complementary techniques. Pull-down assays, gel electrophoresis, and surface plasmon resonance revealed tight binding with sub-micromolar affinity. Cross-linking mass spectrometry with four reagents showed that, within the peptidase, domain D approaches M, C, and S. S is positioned close to M and C, and the peptide contacts all domains. Hydrogen/deuterium exchange mass spectrometry revealed strong and weak protection for C/D and M/S, respectively. Structural analysis by multi-angle laser light scattering and small-angle X-ray scattering in solution revealed that the enzyme adopted highly flexible unbound, latent structures and peptide-bound, active structures that differed from the AD13-MDTCS crystal structure. Moreover, the peptide behaved like a self-avoiding random chain. We integrated the results with computational approaches, derived an ensemble of structures that collectively satisfied all experimental restraints, and discussed the functional implications. The interaction conforms to a 'fuzzy complex' that follows a 'dynamic zipper' mechanism involving numerous reversible, weak but additive interactions that result in strong binding and cleavage. Our findings contribute to illuminating the biochemistry of the vWF:ADAMTS-13 axis.

© 2021 Elsevier Ltd. All rights reserved.

Introduction

Von Willebrand factor (vWF) is a large, abundant multimeric plasma protein mediating blood homeostasis.[1,2] It is synthesized by endothelial cells and megakaryocytes as a polyglycosylated 2813-residue multi-domain pre-pro-protein with a signal peptide, a pro-region, and a mature region. The latter encompasses domains D'-D3-A1-A2-A3 -D4-C1-C2-C3-C4-C5-C6-CK[3] and is secreted into the blood as multimers ranging from dimers to ultra-large ~100-mers (ULVWF). These particles possess potent haemostatic activity and are attached to the endothelium at sites of vascular injury as vWF strings that bridge the subendothelial collagen matrix and receptor complex GPIb-IX-V on the surface of platelets to set off plug formation.[2,4] Under homeostatic conditions, ULVWF is specifically processed to smaller multimers with lower adhesive activity by metallopeptidase (MP) ADAMTS-13 (Figure 1(a)), for which vWF is the only known substrate.[5–8] Impaired ADAMTS-13 function leads to excess vWF activity, which induces thrombi due to aberrant agglutination of platelets in the absence of vascular lesions (Figure 1 (a)).[2,9] Thrombi cause ischaemic stroke, myocardial infarction, thrombotic thrombocytopenic purpura and pulmonary embolism, among other cardio- and cerebrovascular conditions, which collectively are responsible for one in four deaths worldwide.[10–14] By contrast, excessive processing of vWF leads to the bleeding disorders Heyde's syndrome and von Willebrand disease.[15–19]

ADAMTS-13 is a soluble 1398-residue multi-domain protein containing a catalytic domain (domain M, residues A^{75}–A^{293}; numbering in superscript according to UniProt [UP] entry Q76LX8). It is preceded by a signal peptide and a pro-domain (P^{30}–R^{74}) that is removed by furin-type cleavage.[20] In contrast to most metallopeptidases,[21] the pro-domain is not required for latency[20]; instead, the unbound enzyme is inactive and only becomes allosterically activated by substrate binding.[22,23] This latency explains the long half-life of ADAMTS-13 of up to a week in the circulation.[24] The M domain contains the characteristic zinc-binding consensus motif of metzincin MPs (H^{224}-E-X-X-H-X-X-G-X-X-H^{234}) for metal binding and catalysis,[25] and mutation of the general base glutamate to glutamine (E^{225}Q) renders the enzyme incapable of cleaving vWF.[26] The M domain is followed by a disintegrin-like domain (D; G^{294}–P^{379}), a thrombospondin-type 1 repeat (T; I^{380}–E^{439}), a cysteine-rich domain (C; K^{440}–C^{555}), a spacer domain (S; S^{556}–P^{682}), a further seven T-like repeats, and two C-terminal CUB domains.[23,27,28]

Cleavage of vWF by ADAMTS-13 occurs within domain A2 (D_{1498}–V_{1665}; vWF residue numbers in subscript according to UP P04275), exclusively at the Y_{1605}–M_{1606} bond.[29] Notably, the crystal structure of isolated A2 reveals a globular domain in which the cleavage site is not accessible.[30] Indeed, turbulent flow in the bloodstream and shear stress during vWF string-mediated binding and agglutination of platelets triggers unfolding of A2 to expose the scissile bond.[26,31,32] Remarkably, the interaction between A2 and ADAMTS-13 exceeds the M domain because the minimal length of a vWF-derived fragment that mimics the unfolded state of A2 and is cleaved spans 73 residues (D_{1596}–R_{1668}; vWF-peptide, see[33]). Thus, exosites of ADAMTS-13 domains downstream of M must participate in substrate recognition and binding, which explains the strict substrate specificity of the enzyme.[23,28,34] Recognition of E_{1660}-R_{1668} by S, followed by binding of D_{1614} by D through R^{349} and of L_{1603} by the active-site cleft of ADAMTS-13 places the scissile bond for cleaving in what has been dubbed a 'molecular zipper' model.[34,35]
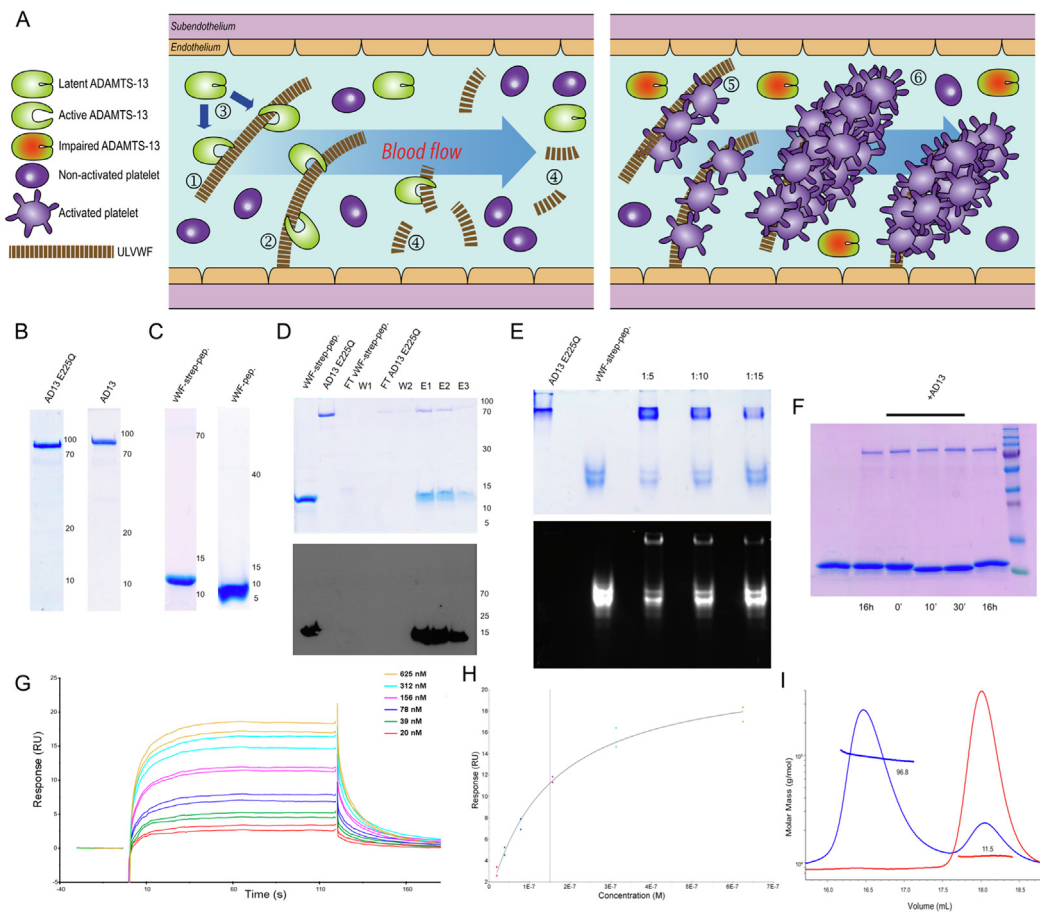
Currently, structural information for ADAMTS-13 at the atomic level is available for the non-catalytic DTCS domains[36] and for a construct spanning domains MDTCS (AD13-MDTCS). The latter is in a substrate-unbound, latent conformation with an occluded active site, which was crystallised with a monoclonal antibody antigen-binding fragment (Fab) owing to the intrinsic flexibility of the molecule.[23] Moreover, structural information based on the M-domain coordinates of ADAMTS-4 and those of the aforementioned non-catalytic domains of ADAMTS-13 has been derived for various constructs in solution by small-angle X-ray scattering (SAXS), which has illuminated how the full-length protein is autoinhibited.[22,28,37]

Herein, the inability to obtain a crystal structure of active ADAMTS-13 in complex with a vWF-derived fragment led us to perform an integrative structural biology approach. We developed high-yield recombinant production systems in human cells for highly active AD13-MDTCS and its inactive AD13-MDTCS-E^{225}Q mutant. We comprehensively characterised its complex with vWF-derived peptides in solution by pull-down assays, gel electrophoresis (including western blotting), proteolytic assays, surface plasmon resonance (SPR), chemical cross-linking followed by mass spectrometry (MS) (CLMS), hydrogen/deuterium exchange MS (H/DXMS), multi-angle laser light scattering (MALLS) after size-exclusion chromatography (SEC), SAXS, and biocomputing. The integration of the data enabled us to propose a working model of the competent complex in solution.

Results and Discussion

Protein production and purification, biochemical binding, and cleavage assays

We produced efficient recombinant expression systems in human Expi293F cells, and purification schemes for AD13-MDTCS and active site point mutant AD13-MDTCS-E^{225}Q, which were

Figure 1. Physiological function of von Willebrand factor, protein production and purification, binding studies, and biochemical assays. (A) Scheme depicting one function of vWF in the circulation. (*Left panel*) Under homeostatic conditions, ULVWF multimers in solution or strings are processed by ADAMTS-13 (① and ②), which transits from a latent to an active conformation upon substrate binding (③). This creates smaller vWF multimers (④) with lower adhesive and thrombogenic activity. (*Right panel*) When ADATMS-13 activity is impaired or deficient, thrombogenic ULVWF multimers accumulate, which favours the activation of platelets (⑤) and augments circulating thrombi (⑥). (B) SDS-PAGE of pure AD13-MDTCS-E^{225}Q (*left*) and AD13-MDTCS (*right*). (C) SDS-PAGE of pure vWF-strep-peptide (*right*) and vWF-peptide (*left*). (D) (*Top panel*) Pull-down assay of vWF-strep-peptide (*lane 1*) and AD13-MDTCS-E^{225}Q (*lane 2*). The peptide was anchored to the resin until saturation (*lane 3*; FT, flow through) and washed (*lane 4*, washing step W1). The peptidase was passed through the column several times (*lane 5*; FT, flow through), and the resin was extensively washed (*lane 6*, washing step W2). The complex was then eluted with biotin-containing buffer (*lanes 7–9*, steps E1–E3). (*Bottom panel*) Western blotting of the above gel on which the vWF-strep-peptide was detected with a streptavidin antibody. (E) (*Top panel*) Coomassie-stained native PAGE of AD13-MDTCS-E^{225}Q (*lane 1*) and fluorophore-labelled vWF-strep-peptide (*lane 2*), as well as incubation of both molecules at three peptidase:peptide molar ratios (*lanes 3–5*). (*Bottom panel*) The previous gel before staining visualized in a fluorescence imaging device to show fluorophore-labelled vWF-strep-peptide in the high-molecular-weight bands in complex with the peptidase. (F) vWF-strep-peptide (*lane 1*) was incubated with AD13-MDTCS-E^{225}Q (*lane 2*), AD13-MDTCS (*lanes 3–5*), or AD13-MDTCS plus EDTA (*lane 6*) according to markers (*lane 7*). The peptide was cleaved after 10 min by active AD13-MDTCS but not in the other reaction mixtures. (G) SPR sensorgrams of the interaction of AD13-MDTCS-E^{225}Q as analyte and vWF-strep-peptide as anchored ligand. Curves from a multi-cycle run at analyte concentrations between 20 nM and 625 nM are depicted, from which the kinetic equilibrium dissociation constant ($K_D = 1.42 \times 10^{-7}$ M) was determined. (H) Plot of the steady-state response values of (G). The vertical line corresponds to the equilibrium dissociation constant ($K_D = 1.50 \times 10^{-7}$ M). (I) SEC-MALLS chromatograms of vWF-strep-peptide (*red curve*) and the AD13-MDTCS-E^{225}Q:vWF-strep-peptide complex (*blue curve*), which reveals an excess of peptide (*right peak*). The respective experimental molecular masses (in kDa) are indicated. The theoretical mass values of the peptide and the complex are 11.2 kDa and ~89 kDa (incl. ~10 kDa glycans), respectively.

obtained in highly pure form with yields of ~1.8 and ~2.0 mg per litre of expression medium, respectively (Figure 1(b)). We also produced vWF-peptide and vWF-strep-peptide, a variant with a C-terminal Strep-tag, in large quantities in a bacterial system as fusion constructs with glutathione S-transferase, which was removed after initial affinity chromatography purification (Figure 1(c)). We performed pull-down assays with vWF-strep-peptide anchored to Strep-Tactin-resin and AD13-MDTCS-E^{225}Q in the liquid phase, followed by SDS-PAGE and western blotting analysis. The proteins coeluted owing to a strong interaction that outcompeted binding to the resin (Figure 1(d)). In addition, fluorophore labelling of the peptide and incubation with AD13-MDTCS-E^{225}Q revealed the presence of the peptide in a fluorescent band migrating according to the mass of the peptidase in native PAGE (Figure 1(e)). This result confirms that the proteins formed a complex that prevails over interactions with the gel matrix. Finally, we analysed cleavage by incubating AD13-MDTCS or AD13-MDTCS-E^{225}Q with the vWF-strep-peptide and found that the former but not the latter completely cleaved the substrate at a single site after 10 min, which suggests that our peptidase preparation is more active than a recently published one from insect cells (see Figure 1(f) in[23]). The cleavage is consistent with the reported processing at Y_{1605}–M_{1606}[29] and was ablated with the general metal chelator EDTA, which inactivates MPs (Figure 1(f)).

Determination of the complex affinity and kinetic parameters
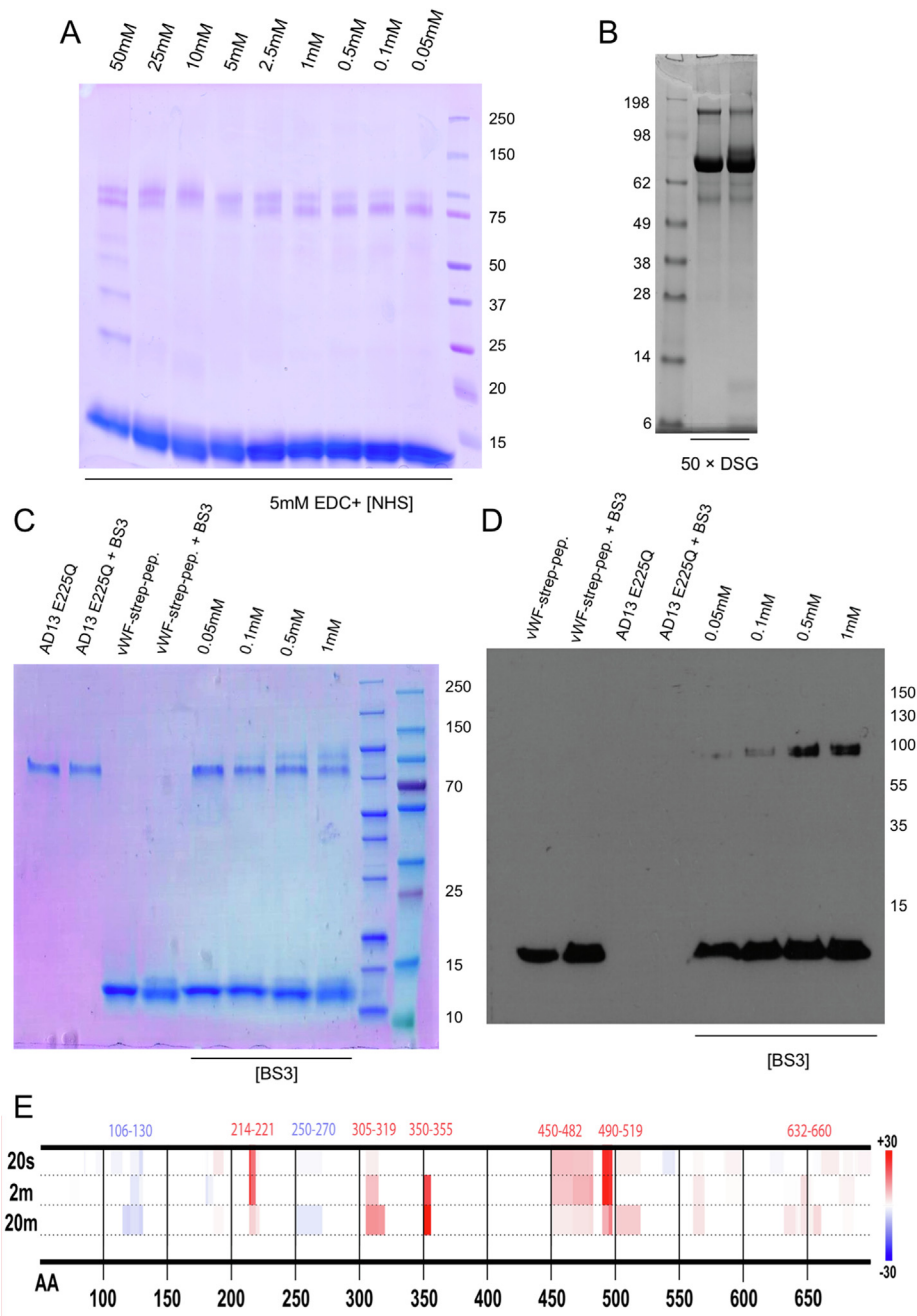
The peptidase:peptide interaction was further investigated by SPR in a multicycle, double-referenced experiment. The vWF-strep-peptide ligand was first immobilised through a Strep-tag on chip-bound Strep-Tactin. Subsequently, binding to the AD13-MDTCS-E^{225}Q analyte was monitored at six serially diluted concentrations. The resulting sensorgrams revealed fast association and dissociation of the binding partners, which indicated high-affinity complex formation (Figure 1(g)). Moreover, the response curves were fitted with an excellent goodness-of-fit ($\chi^2 = 0.81\%$ of R_{max}; U-value = 5). The derived rate constants for association (k_a) and dissociation (k_d) were 5.15×10^5 M^{-1} s^{-1} and 7.28×10^{-2} s^{-1}, respectively, with an estimated dissociation halftime ($t_{1/2}$ = ln2/k_{off}) of 9.5 s and 7.3% complex decay per s. The equilibrium dissociation constants (K_D) from the kinetic and steady-state analysis were 1.42×10^{-7} and 1.50×10^{-7} M, respectively (Figure 1(h)), which are equivalent and signify remarkable sub-micromolar affinity. Overall, the peptide was strongly bound, which is notable for a disordered molecule of this size.

Chemical cross-linking analysis

The interaction was also assessed by CLMS using cross-linking agents EDC/NHS, BS3, DSG, and DSA in separate experiments. The agent DSA in its ^{12}C (light) and ^{13}C (heavy) variants was used for quantitative studies of complex formation. The best conditions for reaction with EDC/NHS and BS3 were 5 mM EDC plus 10 mM NHS and 0.5 mM BS3, respectively (Figure 2(a) and (c)). The latter was verified by western blotting analysis, revealing that even the highest reagent concentration did not cause significant cross-linking of the separate proteins (Figure 2(d)), which excludes binding *in trans* under the assay conditions. The best conditions for DSG and DSA involved 50-fold excess of reagent (Figure 2(b)).

MS analysis of the resulting tryptic peptides revealed 10 (EDC/NHS), 5 (BS3), 4 (DSG) and 3 (DSA) intra-peptidase connections (Supplementary Tables 1 and 2). Remarkably, K^{318}, which is exposed on the D domain, was involved in 12 links in total with residues from the C (Y^{468}, E^{492}, K^{497}, D^{500}, and D^{516}), M (D^{117}, D^{182}, and E^{184}), and S (K^{559}, E^{634}, and D^{635}) domains. Moreover, other cross-links were found between domains M and D (S^{272}–K^{368} and S^{275}–K^{368}), M and S (E^{184}–K^{559}), C and S (E^{492}–K^{559} and K^{497}–K^{608}), and within D (K^{364}–K^{368} and T^{358}–K^{368}), C (K^{441}–T^{435} and T^{453}–K^{440}), and S (K^{559}–T^{575}). Overall, these results indicate that peptide-bound active AD13-MDTCS exhibits great flexibility in solution, which brings D close to M, C, and S, as well as M and C close to S, in agreement with previous reports (see[23,28] and references therein) and the results from H/DXMS (see below). Interestingly, while some of these cross-links are compatible with the unbound latent crystal structure in complex with an Fab fragment (PDB 6QIQ;[23] taking into account some breathing of the hinges between vicinal domains, others require substantial structural rearrangement. This implies that the active structure in solution is significantly different or is highly flexible. Indeed, the ratios between light and heavy peptides obtained with the DSA cross-linker suggest that the peptidase adopts a more compact conformation in the presence of vWF-strep-peptide (Supplementary Figure 1).

Regarding inter-molecular cross-links, experiments with EDC/NHS and DSG but not BS3 or DSA further revealed 11 cross-links in total between S^{266} from M, K^{318} from D, S^{388} from T, K^{497} from C, and K^{559} from S, with vWF residues ranging Y_{1605}–D_{1663} (Supplementary Tables 1 and 2). Remarkably, D was found cross-linked with peptide residues that were previously shown to interact with S.[71,72] This sheds new light on published findings that a monoclonal antibody against S exposes an epitope of another monoclonal antibody against M.[73] Finally, DSG and EDC/NHS produced a link between S^{561} and a residue from the C-terminal Strep-tag. This supports reported

Figure 2. Cross-linking conditions and hydrogen/deuterium exchange mass spectrometry heat map. (A) SDS-PAGE depicting the cross-linking of AD13-MDTCS-E^{225}Q and vWF-strep-peptide after reaction with 5 mM EDC and different concentrations of NHS. (B) Same as (A) but with a 50-fold excess of DSG as cross-linker. *Left lane*, AD13-MDTCS-E^{225}Q; *right lane*, AD13-MDTCS-E^{225}Q:vWF-strep-peptide. (C) Same as (A) but with BS3 as cross-linker. In *lanes 2* and *4*, the concentration of BS3 was 1 mM, which did not cross-link the peptidase and peptide separately. (D) Similar to (C) but showing western blotting analysis using a streptavidin antibody to detect vWF-strep-peptide. Increasing concentrations of BS3 cause more peptide to be bound by the peptidase. (E) Differential deuterium uptake of AD13-MDTCS-E^{225}Q at 20 s, 2 min, and 20 min after incubation with vWF-strep-peptide. The abscissa depicts the residue numbers of the peptidase, and the ordinate shows the percentage of deuterium exchange (from +30% to −30%). Peptidase segments protected by complex formation with the peptide are shown in red. The figure is representative for three independent experiments.

biochemical evidence that S interacts with the C-terminal part of the vWF A2 domain.[36,71,72,74]. Overall, these results indicate that the peptide creeps along the surface of active AD13-MDTCS by contacting all domains.

Surface protection studies

The complex was further studied by H/DXMS (Figure 2(e) and Supplementary Figure 2). The resulting heatmap evinces dynamic protection of the peptidase surface against deuterium exchange by the peptide. The strongest protection is observed in regions L^{350}–L^{355} and C^{450}–K^{497}, which would constitute the main interaction surface of the complex, with secondary interactions involving T^{214}–T^{221}, Y^{305}–A^{319} and I^{645}–E^{651}. These results indicate that the peptidase interacts with the peptide mainly via D and C, and secondarily with M and S, which is overall consistent with the results from CLMS (see above). Moreover, these data are in good agreement with previous reports,[36,75] including the identification of R^{349}-L^{351} as a peptidase exosite[35] and the shielding of C by the peptide.[72]

Latent AD13-MDTCS in solution is flexible and deviates from the crystal structure

While reanalysing SAXS data reported previously for unbound latent AD13-MDTCS in solution,[28] we found that the experimental SAXS profile did not match the theoretical SAXS profile derived from the latent crystal structure (χ^2 = 6.0). This implied substantial rearrangement of the peptidase in solution. Thus, we sampled conformations along the first five nontrivial normal modes (Supplementary Figure 4(a)), which revealed bending and twisting along the T domain while the relative orientations of the M and D domains and C and S domains remained relatively constant. Consistently, three hinge residues were identified in the middle of the T domain (Supplementary Figure 4(b)). We then selected sub-ensembles of conformations sampled along these normal modes that collectively fitted the SAXS data, and found that allowing for flexibility along the hinge points substantially improved the agreement between the coordinates and the experimental SAXS data (χ^2 = 1.8) (Figure 3(a) and (b)). However, some departures from a perfect fit were observed, most probably due to the simplicity of the normal mode description of protein dynamics. Notably, these structures were mainly sampled by one nontrivial normal mode (mode 7), which thus largely accounts for the flexibility of the peptidase in solution (Supplementary Figure 4(c)). The results demonstrate that the unbound latent peptidase is monomeric and flexible in solution, and behaves as two rigid bodies consisting of M and D, and C and S, respectively, connected by a flexible T domain that acts as a hinge.

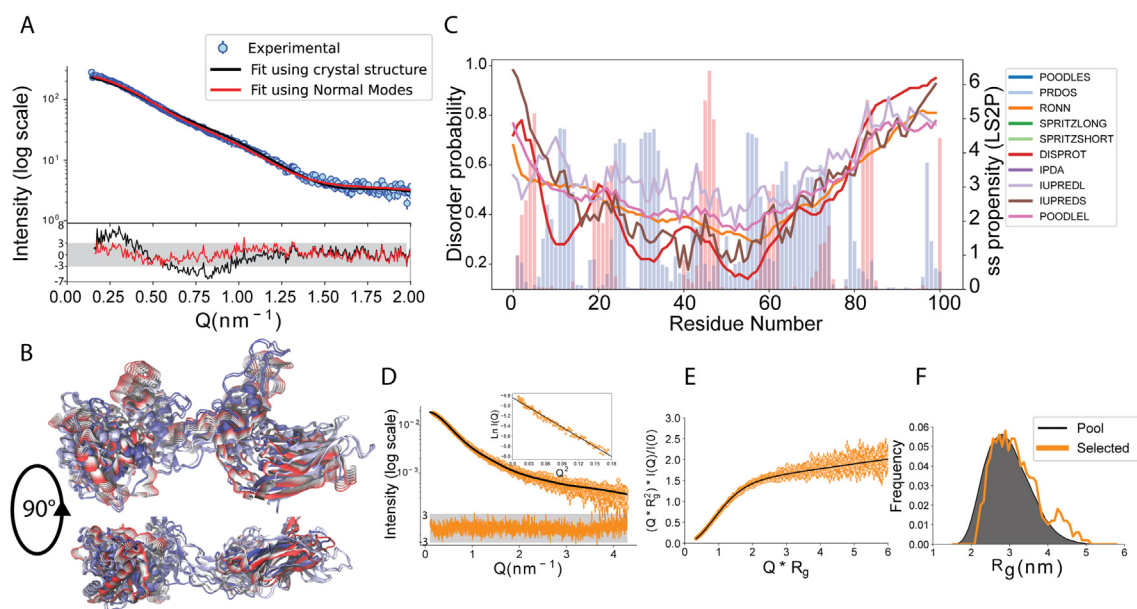### The vWF-strep-peptide is a self-avoiding random chain

Next, we analysed peptide disorder by employing several bioinformatics approaches, which predicted general disorder except for the central region that has some degree of structure, based on transient secondary structure elements (Figure 3(c)). Moreover, assessment of the secondary structure propensity by residue further indicated that the central region is partially structured. Subsequently, we used SAXS to investigate the conformational space sampled by the peptide in solution (Supplementary Table 3). The SAXS intensity profile and Guinier plots at the highest concentration tested are shown in Figure 3(d), and the pairwise distance distribution ($P(r)$) is shown in Supplementary Figure 3. The low-Q range indicates minimal aggregation, as inferred from similar radius-of-gyration (R_g) values for different concentrations (3.08 ± 0.03 nm at 3 mg/mL and 3.04 ± 0.02 nm at 6 mg/mL; Supplementary Table 3). The experimental molecular weight was calculated to be 12.0 ± 1.2 kDa, which matches data from SEC-MALLS (11.5 kDa; Figure 1(i)) and the theoretical molecular weight (11.2 kDa). This indicates that the protein is monomeric in solution, even at high concentration. Finally, the lack of a peak in the normalized Kratky plot further implies that the peptide is disordered (Figure 3(e)).

Interestingly, R_g was higher than expected for an intrinsically disordered protein (2.86 nm) based on Flory's equation.[76] Together with the disorder prediction, this confirms some level of regular structure that results in a more elongated conformation than that expectable for a random chain. Indeed, the Flory exponent of 0.6 calculated using the molecular form factor approach is consistent with a self-avoiding random chain rather than an intrinsically disordered protein.[77] We subsequently generated peptide conformations to select sub-ensembles of 20 conformations that collectively best described the SAXS data for the peptide using the EOM method. The results from one of the cycles are shown in Supplementary Figure 4d, and the corresponding fit to the experimental data is shown in Figure 3(d). The peptide has a broad distribution of R_g values with an average of 3.2 nm (Figure 3(f)). Again, the distribution is slightly shifted toward an extended conformation rather than a pure random coil, which further indicates partial regular secondary structure.

Solution structure of the AD13-MDTCS-E²²⁵Q: vWF-strep-peptide complex

Analysis of the complex by SEC-MALLS revealed a single peak of 96.8 kDa (Figure 1(i)), which is consistent with the theoretical value of ~89 kDa. Next, we collected SAXS data for the peptidase: peptide complex in SEC-SAXS mode (Figure 4(a) and Supplementary Table 3). The extracted profile
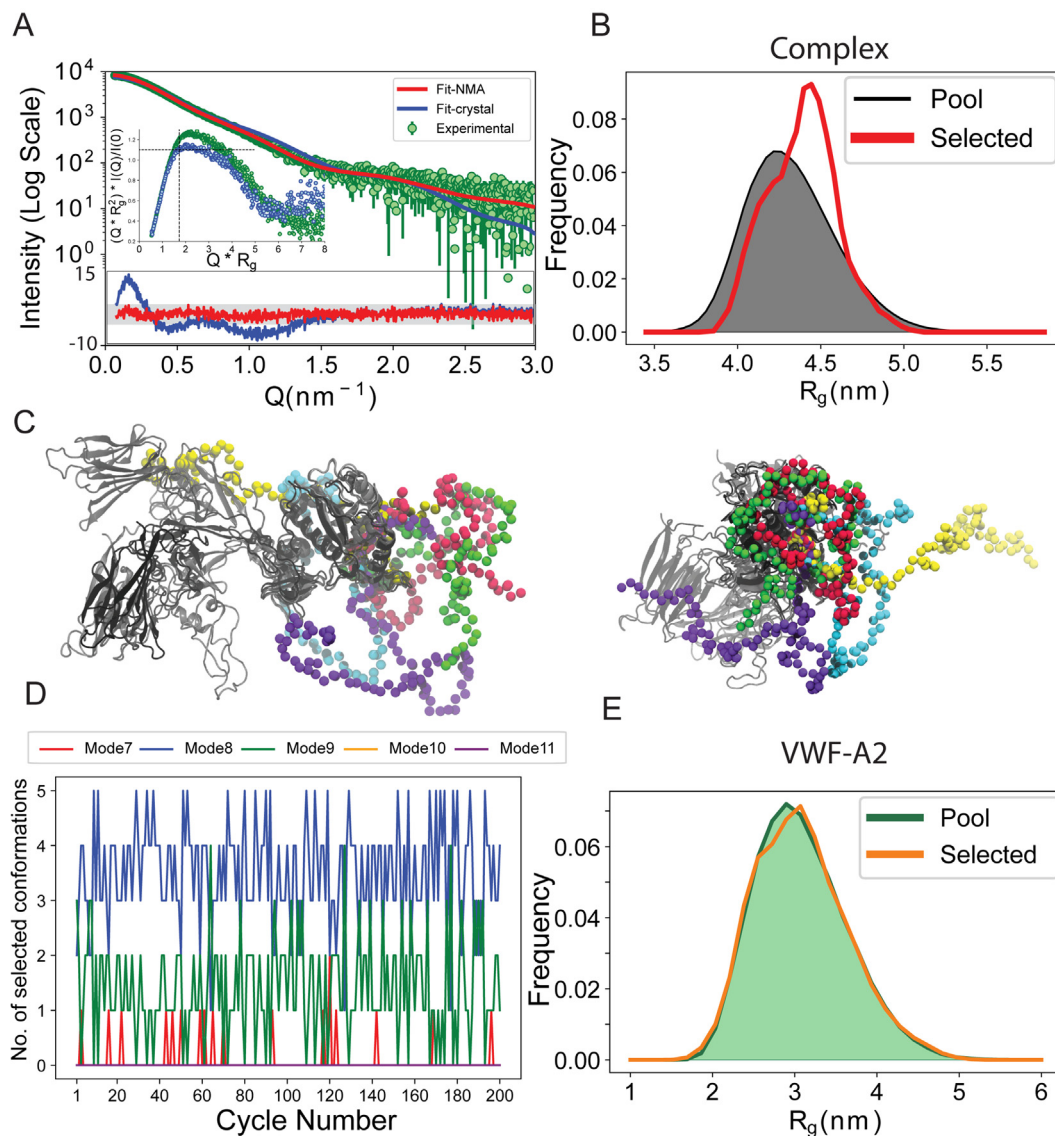
Figure 3. Flexibility of AD13-MDTCS and vWF-strep-peptide in solution. (A) SAXS profile of AD13-MDTCS from[28] along with the theoretical curve computed from the crystal structure (*black*) and the fit obtained using EOM with the conformations sampled along the normal modes (*red*). The residuals are presented at the bottom with the shaded region showing the range of intensities from −3 to +3. (B) Two orthogonal views of the AD13-MDTCS conformations selected by EOM. (C) Disorder assessment of the peptide using different predictors. The bars show the propensity of each residue to adopt an α-helical (*red*) or β-strand (*blue*) conformation. (D) SAXS profiles of vWF-strep-peptide at 6 mg/mL (*orange*). The black line shows the fit obtained using EOM, and the residual plot (*bottom*) reveals the difference between the experimental and the optimised curves. The Guinier plot with the linear fit is shown in the inset (*black line*). (E) Normalized Kratky plot of the profile shown in (D) with the fit using the molecular form factor approach (*black line*). (F) R_g distributions for the initial pool (*black*) and the sub-ensemble selected using EOM (*orange*).

of the complex corresponded to a globular particle (R_g = 4.38 ± 0.01 nm), which is larger than the unbound peptidase (R_g = 3.80 ± 0.05 nm). Consistently, the peak of the normalized Kratky plot was shifted from 2.0 to 2.3 upon complex formation (Figure 4(a)), which implies that the peptidase displays moderate flexibility and that, upon complex formation, an increase in flexibility caused by the peptide is further observed. This finding was substantiated by inspection of the *P(r)* function of the complex, which displays fewer signatures than the peptidase alone (Supplementary Figure 3).

We subsequently performed ensemble modelling. To provide an accurate starting molecular model for the active peptidase, the M domain from the latent crystal structure was remodelled to match active ADAMTS structures while the remaining domains were kept intact. As depicted in Figure 4(a), the ensemble generated with the rigid peptidase model based on the crystal structure did not fit the experimental SAXS profile (χ^2 = 10.1). This was expected given that the unbound latent peptidase in solution already diverged from the latent crystal structure (see above). We then allowed for flexibility by building distinct peptide conformations for each of the conformational ensembles generated for the

isolated peptidase using normal modes (see above), resulting in 120,000 structures of the complex. Subjecting this ensemble to genetic algorithm-based optimization gave an excellent fit to the data (χ^2 = 1.2; Figure 4(a)). The conformations selected in one of the cycles are shown in Figure 4(c). The R_g distribution of the selected pool was quite broad, which supports high flexibility of the complex and a slight preference for more extended structures compared with the total pool (Figure 4(b)).

We also examined the flexibility of the peptidase in the active conformation within the complex by analysing the motional modes sampled by the individual conformations selected with the SAXS data. Interestingly, the ensembles were almost exclusively constituted from modes 8 and 9, with sporadic contributions of mode 7, suggesting that these modes alone largely describe the overall interdomain motions (Figure 4(d)). These results differ from those obtained for the unliganded latent peptidase, where mode 7 made the largest contribution to the selected ensembles, and suggests that peptide binding changes the inherent molecular motions of the peptidase. On the other hand, the R_g distribution of the selected peptide conformations within the complex was almost identical to that of the total pool, which

Figure 4. Solution structure of the AD13-MDTCS-E^{225}Q:vWF-strep-peptide complex. (A) SAXS intensity profile of the complex obtained from SEC-SAXS data (*green*) superposed with the best fit obtained by EOM using a static structure for the peptidase and 10,000 conformations for the peptide (*blue curve*). Further accounting for peptidase flexibility following normal mode analysis provides a much better fit to the data (*red curve*). The normalized Kratky plots for the peptidase (*blue*) and the complex (*green*) are shown in the inset in which dashed lines show the expected position (1.73) and height (1.10) of the theoretical peak for a globular protein. (B) R_g distribution for the total pool (*black curve*) and the selected sub-ensemble (*red curve*). (C) Two orientations (*left* and *right*) of the EOM-selected conformations that collectively describe the experimental SAXS data. (D) Contribution of the individual modes to the selected sub-ensemble for 200 cycles of EOM. (E) Comparison of the R_g distribution of peptide conformations bound to the peptidase in the complete pool (*green curve*) of the complex and the sub-ensemble selected by EOM (*orange curve*).

indicated no preferential selection of the peptide in terms of size or extension (Figure 4(e)). Thus, the peptide displayed a similar degree of disorder to the unbound state upon complex formation. This observation also indicates that the putative occurrence of multiple simultaneous binding events suggested by the 'molecular zipper'

model[23,34] must be transient in nature, and SAXS is not sensitive enough to detect them.

Validation of the complex structure

We next analysed the compatibility of the inter-molecular distance restraints resulting from CLMS (Supplementary Table 1) with the SAXS-derived

structure ensembles. We filtered the total pool of structures and retained only those in which the peptidase is in a conformation selected by at least one of the EOM cycles. Such filtering was not required for the peptide due to its much higher flexibility (see above). The positions of the Cα atoms of the cross-linked amino acids of the peptide and the peptidase, for which cross-linking was observed, are shown individually in Supplementary Figure 5. The high flexibility of the peptide in the complex is evidenced by the large space explored by these individual residues, which systematically increases with the distance between the cross-linked amino acids and the docked peptide. In all cases, we found overlap between the spaces explored by the pairs of cross-linked residues. Therefore, the CLMS data are compatible with the structural model of the complex derived from SAXS data and computational methods.

A working model for the functional AD13-MDTCS:vWF-strep-peptide complex in solution

To generate molecular models for the competent complex, we selected peptidase conformations identified at least once by EOM from the SAXS data, and calculated peptides in random-coil conformation. Using a genetic algorithm-based selection, we acquired sub-ensembles of five conformations that agreed with all the experimental CLMS restraints, one of which is presented in Figure 5(a). Running the genetic algorithm multiple times yielded different, equally valid sub-ensembles, which indicates that there are multiple ways in which the proteins may interact. It is also important to note that these sub-ensembles alone do not fit the SAXS data but represent minimal clusters that collectively fulfil all the distance restraints.

We subsequently constructed a full-atom model for one of the conformers of this sub-ensemble (Figure 5(c)). Superposition of the M domain onto that of the latent crystal structure (Figure 5(b)) reveals that D is very close in both structures, with a maximal deviation of ~3 Å. A rotation of ~10° around P^{379} within the linker between D and T causes a maximal displacement of ~10 Å for S^{399} in the distal part of the latter domain. Furthermore, the TC linker contains a hinge point, and a ~17° rotation about A^{437} leads to a maximal deviation of ~6 Å at H^{476}. Finally, only a small rearrangement is observed between C and S. Overall, these changes lead to a maximal displacement of ~47 Å at the most distal part of S (Figure 5(b)).

Conclusions

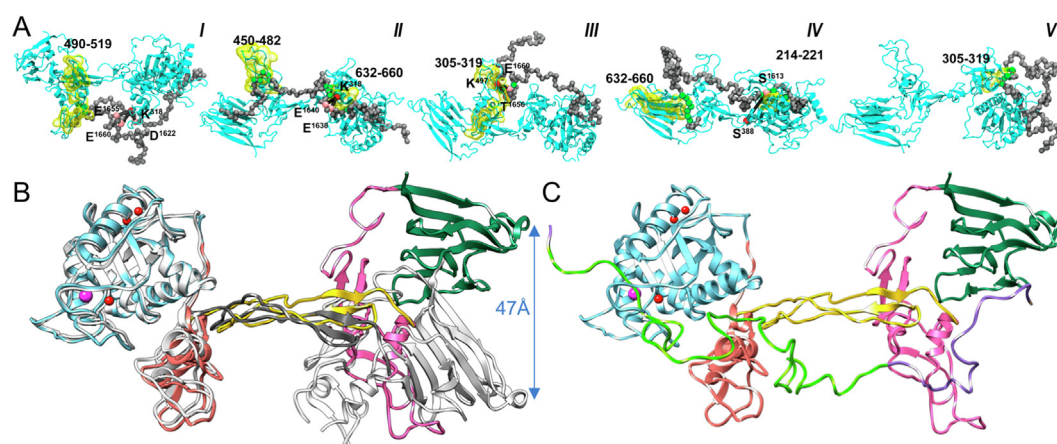The molecular details of the complex formed between active AD13-MDTCS and its cognate region of the vWF A2 domain encompassing the scissile bond have proved difficult to elucidate using classical structural methods for years. Previous studies identified several binding sites on the enzyme surface that are bound by the unfolded A2 domain of vWF. Binding to these exosites, which transcend the M domain, positions the peptide within the active site cleft in the correct conformation and orientation for cleavage in what has been dubbed a 'molecular zipper' model.[23,34] Herein, we set out to comprehensively analyse the peptidase:peptide interaction through an integrative structural biology approach, applying nine complementary biophysical, biochemical and biocomputational techniques.

SAXS and SEC-MALLS analyses demonstrated that the isolated proteins are highly flexible in solution. This plasticity is maintained in the complex, which therefore cannot be recapitulated by a single, rigid structure but rather conforms to a 'fuzzy complex.' Such complexes often link regulation to protein dynamics.[78,79] This further implies that binding of the peptide to the peptidase, which involves specific residue pairs and protected regions identified by CLMS and H/DXMS, respectively, is transient in nature. Thus, the high binding affinity and very efficient cleavage observed in gel-electrophoresis, pull-down, SPR, and peptidolysis assays are the result of multiple low-affinity interactions and small individual energy contributions that simultaneously populate the interaction sites in a variety of ways. Counterintuitively, the complex remains highly disordered while driving the peptide in the optimal orientation for catalysis. This property is characteristic of intrinsically disordered proteins, which comprise several consecutive polypeptide stretches that recognize multiple partners or multiple sites of the same partner.[80] This feature enables cooperative binding while preserving plasticity, which reduces the entropic cost of the interaction. Overall, the ADAMTS-13: vWF-peptide interaction revealed herein appears to conform to a 'dynamic zipper' mechanism, consistent with previous studies showing that modifying individual exosites of the peptidase only moderately reduces the affinity for, and cleavage of, the peptide.[23,34]

Materials and Methods

Expression and purification of recombinant AD13-MDTCS and AD13-MDTCS-E^{225}Q

A cDNA encoding AD13-MDTCS fragment A^{75}–A^{685} was amplified from plasmid pcDNA4/TO[38] and cloned between *Sma*I and *Not*I (Thermo Fisher Scientific) restriction sites of a modified pCMV-SPORT6 vector using three forward primers for consecutive PCR amplifications (5′-CTGGGTTCC AGGTTCCACTGGTGACGCTGCAGGCGGCATC CTA-3′, 5′-TCCTGCTATGGGTACTGCTGC TCT GGGTTCCAGGTT-3′, and 5′-ATGGAGACAGACA CACTCCTGCTATGGGTA-3′) and reverse primer 5′-GCATGCGGCCGCAAGCTTATTAG-3′

Figure 5. Integrative atomic model of the AD13-MDTCS-E^{225}Q:vWF-strep-peptide complex. (A) Example of a sub-ensemble of five complex structures (I–V) selected by artificial intelligence that fulfils all the 11 inter-molecular cross-linking restraints (Supplementary Table 1). AD13-MDTCS is shown as cyan ribbons and vWF-strep-peptide as a grey string of beads, each representing a Cα atom. Black cylinders connect the cross-linked Cα atoms. The surfaces that are protected in H/DXMS experiments are coloured in yellow, and peptide residues that confer protection in H/DXMS experiments are shown as green spheres. These residues lie within ~5 Å of the protected surface. In this particular ensemble, the CLMS data can be explained with three structures, while fulfilment of H/DXMS data requires two additional structures. (B) Ribbon-type plot of the peptidase moiety of model II of (A), which fulfils 7/11 of the experimental inter-molecular CLMS restraints (see also Supplementary Table 1), with the M, D, T, C, and S domains coloured in sky blue, salmon, gold, hot pink, and sea green, respectively. The zinc ion is coloured magenta, and calcium ions are red. The M domain of the model is superposed onto the crystal structure of latent AD13-MDTCS-E^{225}Q (M, D, C, and S in white, T in grey). The largest distance is found between the respective Y^{605} residues (*blue arrow*). (C) Ribbon plot of the peptidase:peptide complex in the orientation shown in (B). The peptide is represented as a green coil for segment D$_{1598}$–R$_{1668}$, and residues upstream and downstream of the construct are coloured purple.

(all purchased from Sigma-Aldrich). The resulting pS6-AD13-MDTCS plasmid contained the signal peptide from the V-J2-C region of a mouse Ig κ-chain instead of the native leader sequence, and a C-terminal human rhinovirus 3C proteinase cleavage site plus a hexahistidine (His$_6$)-tag. Thus, the resulting protein comprised residues D+A^{75}–A^{685}-+LEVLFQGPHHHHHH. This construct was used to generate A13-MDTCS-E^{225}Q (plasmid pS6-AD13-MDTCS-E225Q) via the QuikChange Site-Directed Mutagenesis Kit (Agilent Technologies) with forward primer 5′-AGTCACCATTGCCCATCA GATTGGGCACAG-3′ and reverse primer 5′-CTGTGCCCAATCTGATGG GCAATGGTGACT-3′. PCR amplifications were performed with Phusion High Fidelity DNA polymerase (Thermo Fisher Scientific), plasmids were purified with the Gene-JET Plasmid MaxiPrep Kit (Thermo Fisher Scientific), and constructs were verified by DNA sequencing.

Human Expi293-F cells (Thermo Fisher Scientific) adapted to FreeStyle F17 expression medium (Gibco) were grown at 37 °C to a density of 3–5 × 10^6 cells/mL in a Multitron Cell Shaker Incubator (Infors HT) at 150 rpm in a humidified atmosphere with 8% CO$_2$, and sub-cultured every 3–4 days by dilution to 0.3–0.5 × 10^6 cells/mL. Cells were then sub-cultured to 0.7 × 10^6 cells/mL in medium containing penicillin/streptomycin, 0.5

μg/mL amphotericin, 8 mM L-glutamine, and 0.2% Pluronic F-68 (Gibco). After 24 h, cells at a density of 1 × 10^6 cells/mL were transfected with 1 mg vector DNA and 3 mg linear 25 kDa polyethyleneimine (Polysciences Europe) in 20 mL Opti-MEM medium (Gibco), previously incubated at room temperature for 15–20 min, per litre of expression medium. After 3 days, the cell culture supernatant was harvested, cleared at 4 °C by centrifugation at 3500g for 30 min, and filtered through a 0.45 μm cellulose acetate filter (Millipore).

The supernatant was then supplemented with 15 mM imidazole, incubated with nickel-nitrilotriacetic acid resin (Ni-NTA; Invitrogen) for 3–4 h, loaded onto a Poly-Prep open column (Bio-Rad) for batch affinity chromatography purification, and washed extensively with 50 mM Tris·HCl pH 7.4, 250 mM sodium chloride, 50 mM L-arginine, 50 mM L-glutamine, 20 mM imidazole. The protein was eluted with the same buffer containing 300 mM imidazole, and fractions were pooled and desalted with the same buffer without imidazole using a PD10 column (Sigma-Aldrich). The sample was concentrated and subjected to SEC on a Superdex 200 10/300 column (GE Healthcare) attached to an ÄKTA Purifier liquid chromatography system (GE Healthcare) operated at room temperature. Protein purity and identity were assessed by 12% glycine SDS-

PAGE stained with Coomassie Brilliant Blue (Thermo Fisher Scientific), as well as peptide mass fingerprinting and N-terminal sequencing at the Protein Chemistry Service and the Proteomics Facility of the Centro de Investigaciones Biológicas (Madrid, Spain), respectively. Ultrafiltration steps were performed with Vivaspin 15 and Vivaspin 2 filter devices with a 10 kDa cutoff (Sartorius Stedim Biotech). Approximate protein concentrations were determined by measuring the absorbance at 280 nm (A_{280}) in a spectrophotometer (NanoDrop), and applying the theoretical extinction coefficient. Purified proteins were concentrated and dialysed against 10 mM HEPES pH 7.4, 150 mM sodium chloride for subsequent studies.

Expression and purification of recombinant vWF-peptide and vWF-strep-peptide

A synthetic gene (GeneScript) encoding vWF-peptide (D_{1596}–R_{1668}), codon-optimised for expression in *Escherichia coli*, was amplified with forward primer 5′-ATGCCCATGGAAGATCGT GAGCAA-3′ and reverse primer 5′-GCATCTC GAGTTAACGTTGCAGAACCA-3′, and introduced into the pCri-6b vector[39] between *Nco*I and *Xho*I restriction sites. The resulting plasmid (pCri6b-vWF-pep) conferred kanamycin resistance and attached an N-terminal His$_6$-tagged glutathione S-transferase moiety plus a tobacco etch virus endopeptidase (TEV) cleavage site. An extra C-terminal Strep-tag was introduced by consecutive PCR amplifications to generate vWF-strep-peptide (plasmid pCri6b-vWF-strep-pep) using forward primer 5′-ATGCCCATGGAAGATCGTGAGCAA-3′ and reverse primers 5′-TTCGAATTGTGGATGGC TCCAACCTCCACGTTGCAGAACCAGGT-3′, 5′-A CTTCCACCTCCAGAACCTCCACCCTTTTCGAA TTGTGGATGG-3′, 5′-AATTGTGGATGGCTCCAT GCGCTACCTCCACTTCCACCTCCAGAA-3′, and 5′- GCATCTCGAGCTA CTTTTCGAATTGTGGAT GGCTCCA-3′. The plasmids were separately transformed into *E. coli* BL21 (DE3) cells (Novagen), which were grown at 37 °C in Luria Bertani medium supplemented with 30 μg/mL kanamycin. Cultures were induced at an A_{600} of ~0.8 with 0.4 mM isopropyl-β-*D*-thiogalactopyranoside and incubated overnight at 20 °C. Cell cultures were centrifuged at 5000*g* for 20 min at 4 °C, the pellet was washed with 50 mM Tris·HCl pH 8.0, 150 mM sodium chloride, resuspended in the same buffer plus 20 mM imidazole, and supplemented with cOmplete EDTA-free inhibitor cocktail tablets and DNase I (both Roche Diagnostics). Cells were lysed with a cell disruptor (Constant Systems) at 1.35 kbar, and the cell debris was removed by centrifugation at 20,000*g* for 30 min at 4 °C.

The supernatant containing the fusion construct of vWF-peptide was subsequently filtered and loaded onto a 5-mL Ni-NTA HisTrap HP column (GE Healthcare), and the protein was eluted with a 20–500 mM imidazole gradient in 50 mM Tris·HCl pH 8.0, 150 mM sodium chloride. For the vWF-strep-peptide, the Ni-NTA step was replaced with affinity chromatography using Strep-Tactin XT Superflow Suspension resin (IBA Life Sciences), with elution buffer 100 mM Tris·HCl pH 8.0, 150 mM sodium chloride, 50 mM biotin (VWR Life Science). Subsequently, samples were dialysed overnight at 4 °C against 20 mM Tris·HCl pH 8.0, 150 mM sodium chloride, 1 mM dithiothreitol (DTT) in the presence of His$_6$-tagged TEV at an enzyme-to-sample molar ratio of 1:100. TEV cleavage left additional residues at the N-terminus of both vWF-peptide and vWF-strep-peptide, which spanned residues GAME+D_{1596}–R_{1668} and GAME+D_{1596}–R_{1668}+GGWSHPQFEKG GGSGGGSGGWSHPQFEK, respectively. Digested samples were passed several times through Ni-NTA resin, previously equilibrated each time with 50 mM Tris·HCl pH 8.0, 150 mM sodium chloride, 20 mM imidazole, to trap His$_6$-tagged molecules, and the flow-through containing molecules without His$_6$-tag was collected. Samples were pooled and dialysed overnight against 20 mM Tris·HCl pH 8.0 and further purified by ion-exchange chromatography in a TSK gel DEAE-2SW column (TOSOH Bioscience) operated with a 2–50% gradient of 1 M sodium chloride in 20 mM Tris·HCl pH 8.0 applied over 40 mL. Samples were collected, pooled, concentrated by ultrafiltration, and subjected to SEC on a Superdex 75 10/300 column. The peptides were further analysed by Coomassie-stained 15% tricine SDS-PAGE. Ultrafiltration steps were performed using Vivaspin 15 and Vivaspin 500 filter devices with a 3 kDa cutoff (Sartorius Stedim Biotech).

Pull-down assays and western blotting analysis

vWF-strep-peptide was incubated with Strep-Tactin resin previously equilibrated in 100 mM Tris·HCl pH 8.0, 150 mM sodium chloride for 10 min at room temperature, and then loaded onto a Poly-Prep open column (Biorad). Then, AD13-MDTCS-E^{225}Q at 0.4 mg/mL in 50 mM Tris·HCl pH 7.4, 250 mM sodium chloride was passed several times through the column. After extensive washing with 100 mM Tris·HCl pH 8.0, 150 mM sodium chloride, the complex was eluted with the same buffer plus 50 mM biotin and analysed by 12% tricine SDS-PAGE. Gels were transferred to Hybond ECL nitrocellulose membranes (GE Healthcare) and blocked for 2 hours under gentle stirring at room temperature with 50 mL phosphate-buffered saline (PBS) plus 0.1% Tween 20 and 5% bovine serum albumin (BSA). vWF-strep-peptide was detected with the Streptavidin Peroxidase Conjugated Antibody from *Streptomyces avidinii* (Sigma-Aldrich) diluted 1:1000 in PBS plus 0.1% Tween 20 and 1% BSA.

Complexes were detected using a Super Signal West Pico Chemiluminescent enhanced chemiluminescence system (Pierce). Membranes were exposed to Hyperfilm ECL films (GE Healthcare).

SEC followed by MALLS

Binding of vWF-strep-peptide to AD13-MDTCS-E^{225}Q was assessed at a 10:1 molar ratio by SEC-MALLS at the joint IBMB/IRB Automated Crystallography Platform, Barcelona Science Park (Catalonia, Spain) as previously described for other proteins.[40,41] Briefly, a Dawn Helios II apparatus (Wyatt Technologies) was used, which was coupled to a SEC Superose 6 10/300 column equilibrated in 10 mM HEPES pH 7.4, 150 mM sodium chloride at 25 °C. All experiments were performed in triplicate, and the ASTRA 7 software (Wyatt Technologies) was used for data processing and analysis, for which a dn/dc value typical for proteins (0.185 mL/g) was assumed.

Fluorogenic binding assay

vWF-strep-peptide was labelled with an amine-reactive fluorophore (sulfosuccinimidyl-7-amino-4-methylcoumarin-3-acetate; Thermo Fisher Scientific) in 10 mM HEPES pH 7.4, 150 mM sodium chloride at tenfold molar excess of reagent for 1 h at room temperature according to the manufacturer's instructions. Thereafter, the peptide was extensively dialysed against the same buffer to remove non-reacted dye, and mixed with AD13-MDTCS-E^{225}Q at peptidase:peptide molar ratios of 1:5, 1:10, and 1:15. Reaction mixtures were incubated for 1 h at 37 °C and subsequently analysed by 12% native PAGE. Fluorescence (λ_{ex} = 345–350 nm and λ_{em} = 440–460 nm) was visualised with a G:BOX F3 Gel Doc System gel reader (Syngene), and gels were thereafter stained with Coomassie.

Proteolytic cleavage of vWF-strep-peptide by AD13-MDTCS

AD13-MDTCS and AD13-MDTCS- E^{225}Q in 25 mM Tris·HCl pH 7.5, 250 mM sodium chloride were preincubated in a 100 μL reaction volume with 5 mM calcium chloride and 250 μM zinc chloride (final concentration) for 10 min at 37 °C. vWF-strep peptide in 20 mM Tris·HCl pH 7.4, 150 mM sodium chloride was subsequently added at a peptidase:peptide weight ratio of 1:10 in the absence or presence of 10 mM EDTA. Reactions were stopped at specific time points by boiling aliquots in reducing/denaturing buffer, and samples were further analysed by 15% tricine SDS-PAGE with Coomassie staining.

SPR data acquisition, processing and kinetic data analysis

Binding studies of AD13-MDTCS-E^{225}Q and vWF-strep-peptide were analysed using a Biacore T200 biosensor system (GE Healthcare) at the Scientific and Technological Centres of the University of Barcelona (Catalonia, Spain). Protein Strep-Tactin (IBA LifeSciences) was immobilised on the surface of the four flow cells of a CM5 series S sensor chip (GE Healthcare) through amine coupling as described by the manufacturer. Briefly, the chip was activated by injection of 50 mM N-hydroxysuccinimide and 200 mM N-ethyl-N'-(dimethylaminopropyl)carbodiimide at a flow rate of 10 μL/min for 10 min. Strep-Tactin at 50 μg/mL in 10 mM sodium acetate pH 5.0 was injected over the sensor surface at 5 μL/min for 10 min. Following this procedure, 3000 resonance units (RU) of Strep-Tactin were immobilized on the sensor surface. Excessive reactive groups on the sensor chip were deactivated with 1 M ethanolamine hydrochloride pH 8.5 at 10 μL/min for 10 min. vWF-strep-peptide as ligand in running buffer (10 mM HEPES pH 7.4, 150 mM sodium chloride, 0.05% Tween 20) was bound to Strep-Tactin at 25 °C at low density (20 RU) and a flow rate of 5 μL/min. AD13-MDTCS-E^{225}Q as the analyte was dialysed against 10 mM HEPES pH 7.5, 150 mM sodium chloride, filtered, subjected to twofold serial dilutions (625 nM to 20 nM), and injected at 30 μL/min for 120 s. The association and dissociation phases of the complex were monitored over 90 s to determine the respective rate constants k_a and k_d. After each round of measurements, the sensor chip surface was regenerated by washing with 3 M guanidine hydrochloride at 30 μL/min for 30 s to remove the ligand. These experiments were double-referenced so that the final signal was the measured signal minus the reference signal (flow cell without ligand) and the signal at analyte concentration zero. The overall equilibrium dissociation constant (K_D) was determined by plotting the binding responses in the steady-state region of the sensorgrams (R_{eq}) against analyte concentrations. The constant was also calculated from the ratio of the association and dissociation rate constants ($K_D = k_d/k_a$). Sensorgrams were analysed with the BIAevaluation program (version 3.1; GE Healthcare) and fitted to a 1:1 Langmuir interaction model using global curve fitting analysis. The goodness-of-fit was assessed through the χ^2 statistical parameter and the U-value.

CLMS data acquisition and processing

In a first set of experiments, cross-linking of the AD13-MDTCS-E^{225}Q:vWF-strep-peptide complex was performed either with 5 mM 1-ethyl-3-(3-dimethylaminopropyl)carbodiimide (EDC; Pierce) plus increasing amounts of N-hydroxysulfosuccinimide

(NHS; Sigma; 50 μM to 50 mM) or with bis(sulfosuc cinimidyl)suberate (BS3; Pierce; 1 μM to 1 mM) in 10 mM HEPES pH 7.4, 150 mM sodium chloride. For EDC/NHS, peptidase at 15 μg/mL and peptide at 300 μg/mL were incubated with NHS for 15 min at room temperature. Subsequently, EDC was added to a final concentration of 5 mM and incubated for a further 2 h at room temperature. For BS3, peptidase at 50 μg/mL was incubated with peptide at 300 μg/mL at 4 °C for 45 min. Reactions were subsequently quenched with 2 M Tris·HCl pH 8.0 to a final concentration of 50 mM. EDC/NHS- and BS3-treated samples were assessed by 12% glycine-gradient SDS-PAGE. Reaction with BS3 was further verified by western blotting (see above). The best results were obtained with 0.5 mM BS3 after 45 min at 4 °C and with 5 mM or 10 mM EDC/NHS after 2 h at room temperature, respectively.

Cross-linked proteins were prepared for MS by in-gel digestion as described previously.[42] Briefly, SDS-PAGE bands corresponding to the complex were excised from the gel and dehydrated with acetonitrile. Dried bands were incubated with a 1:1 mixture of 100 mM ammonium bicarbonate and acetonitrile for 15 min, dried in a SpeedVac vacuum centrifuge concentrator (Savant), and digested overnight with 25 ng/mL trypsin (Promega) in 30 μL 50 mM ammonium bicarbonate. The resulting tryptic peptides were desalted with Empore C18 SPE Disks (from 3 M) packed in 10 μL pipette tips.[43] The cross-linked complex was also digested in solution. Reaction mixtures were dried in a SpeedVac vacuum concentrator (Thermo Fisher Scientific) and denatured in 100 mM ammonium bicarbonate, 8 M urea, 10 mM DTT. Subsequently, samples were alkylated with 30 mM iodoacetamide for 30 min at room temperature in the dark, diluted to a final urea concentration of 1 M with 100 mM ammonium bicarbonate, and subsequently digested with 10 μg trypsin overnight at 37 °C. The reaction was stopped through acidification of the sample to pH < 2.5 with formic acid. Tryptic peptides resulting from either digestion procedure were separated by strong cationic exchange (SCX) coupled to reversed-phase chromatography. Specifically, SCX column material (PolyLC) was dissolved in 0.1% formic acid and loaded onto a pipette-tip with an Empore C18 SPE Disk. Peptides were separated with a stepwise sodium chloride gradient (50–600 mM) and subsequently eluted with 70% 0.1% formic acid in acetonitrile for analysis. The micro-purified peptides were then subjected to LC-MS/MS analysis using an EASY nLC-1000 liquid chromatography column (Thermo Fisher Scientific) connected to an Orbitrap QE+ mass spectrometer (Thermo Fisher Scientific). Samples were injected, trapped, and desalted isocratically on a fritted precolumn (100 μm × 2 cm inner diameter) packed in-house with RP ReproSil-Pur C18-AQ 3 μm resin. Peptides were

eluted and separated on a 15 cm analytical column of 75 μm inner diameter packed with the same resin using a 30 min gradient (5–35%) of 0.1% formic acid in acetonitrile at a flow rate of 250 nL/min. Cross-linked peptides were identified with the MeroX software.[44] The results from three independent parallel experiments were combined.

A second set of experiments was performed with disuccinimidyl glutarate (DSG; Creative Molecules) as cross-linking agent. AD13-MDTCS-E^{225}Q and vWF-strep-peptide (1:5 molar ratio) at 1 mg/mL in 10 mM HEPES pH 7.6, 150 mM sodium chloride was mixed with freshly prepared DSG at 50-fold molar excess and incubated for 1 h at room temperature. For quantitative studies, the peptidase:peptide complex, as well as AD13-MDTCS-E^{225}Q alone, were incubated with a 50-fold molar excess of light (^{12}C) or heavy (^{13}C) disuccinimidyl adipate (DSA; Creative Molecules). After a 30 min incubation at room temperature, AD13-MDTCS-E^{225}Q labelled with ^{12}C or ^{13}C DSA and the complex labelled with ^{13}C or ^{12}C DSA, respectively, were mixed at a 1:1 ratio.

For DSG-mediated cross-linking, samples were separated by 4–12% Bis-Tris NuPAGE, and bands corresponding to the linked complex were excised. Cysteines were reduced with 50 mM DTT and then alkylated with 100 mM iodoacetamide in the dark. AD13-MDTCS-E^{225}Q was in-gel deglycosylated with PNGase F (New England BioLabs) at 37 °C overnight, followed by digestion with trypsin at a sample:peptidase weight ratio of 20:1, also overnight at 37 °C. For DSA-mediated cross-linking, proteins in solution were reduced with 10 mM DTT, alkylated with 30 mM iodoacetamide, and digested overnight with trypsin at 37 °C. Peptides were injected onto a Luna Omega 5 μm Polar C18 100 Å 20 × 0.3 mm column (Phenomenex) and desalted at 20 μL/min for 5 min. Peptides were then separated through reversed-phase chromatography with a Luna Omega 3 μm Polar C18 100 Å 150 × 0.3 mm column (Phenomenex) at 10 μL/min using a UHPLC 1290 Infinity II chromatography system (Agilent Technologies) with a gradient sequence of 1–10% for 1 min, 10–45% for 19 min, and 45–95% for 5 min of solvent A (0.1% formic acid, 98% acetonitrile in water) in solvent B (0.1% formic acid, 2% acetonitrile in water). The column was heated to 50 °C and directly connected to a 15 T SolariX XR FT-ICR mass spectrometer (Bruker Daltonics) with an electrospray ion source. Cross-linked peptides were identified with the StavroX software,[45] which was set to account for fixed carbamidomethylation of cysteines and variable methionine oxidation. DSG was assumed to react with N-termini, lysines, serines, threonines, and tyrosines. The mass error threshold was set to 2 ppm, and all assigned fragments were manually curated. For quantitative studies, the Links software[46] was used for identification of cross-linked peptides.

Non-overlapping isotopes of peptides cross-linked with ^{12}C and ^{13}C DSA were used to calculate isotope ratios. All experiments were performed in triplicate.

H/DXMS data acquisition and processing

AD13-MDTCS-E^{225}Q at 300 pM in 10 mM HEPES pH 7.6, 150 mM sodium chloride, with or without a 10-fold molar excess of vWF-strep-peptide, was labelled using 10-fold dilutions in 10 mM Hepes pD 7.6 in D_2O plus 150 mM sodium chloride, and incubated at room temperature for 20 s, 2 min, and 20 min. Reaction mixtures were quenched by instant acidification with 1 M glycine pH 2.3, 6 M urea, 800 mM tris(2-carboxyethyl) phosphine at a 1:1 volume ratio, and immediately flash-frozen in liquid nitrogen. Prior to analysis, samples were thawed and manually injected onto a nepenthesin-2 column. After a 3 min digestion and desalting with a Luna Omega 5 μm Polar C18 100 Å 20 × 0.3 mm column (Phenomenex) and an isocratic pump delivering 0.4% formic acid in water at 400 μL/min, peptides were separated on a Luna Omega 1.6 μm Polar C18 100 Å 100 × 1.0 mm column (Phenomenex) with a linear 10–35% gradient of solvent C (0.4% formic acid, 95% acetonitrile in water) in solvent D (0.4% formic acid, 2% acetonitrile in water) over 12 min. In-column digestion, desalting, and separation were carried out in ice bath to reduce back-exchange. Peptides were detected using a 15 T SolariX XR FT-ICR mass spectrometer operating in positive mode, and data were processed with the DataAnalysis software (version 4.2; Bruker Daltonics) and the in-house DeutEX software.

Protein disorder analysis

The disorder propensity of vWF-strep-peptide was assessed *in silico* using POODLE-S and POODLE-L,[47] PrDOS,[48] RONN,[49] Spritz-L and Spritz-S,[50] IUPred-L and IUPred-S,[51] DISpro, and iPDA[52] through the Genesilico MetaDisorder web server.[53] In addition, the secondary structure propensity of each residue was calculated by the LS2P method.[54]

SAXS data acquisition and processing

Samples were prepared in 10 mM HEPES pH 7.4, 150 mM sodium chloride, and scattering data were collected at beamline P12 of the Petra III storage ring of the Deutsches Elektronensynchrotron (DESY) in Hamburg (Germany) at 20 °C. The isolated vWF-strep-peptide was analysed at 3 and 6 mg/mL in 40 μl volumes. Data were collected in batch mode in 40 frames of 45 ms exposure flanked by two exposures of the buffer, and were subjected to radial averaging, background subtraction, and merging using the SASFLOW pipeline.[55] For the AD13-MDTCS-E^{225}Q:peptide complex (1:10 molar ratio), data at 1.5–6.0 mg/mL concentration were collected using size-exclusion chromatography coupled to SAXS (SEC-SAXS) and processed using the CHROMIXS program.[56] This included selection of the frames corresponding to protein and buffer, buffer subtraction and averaging. The SAXS profiles obtained from either batch mode or SEC-SAXS were analysed using the ATSAS suite of programs.[57] Moreover, reported SAXS data for wild-type AD13-MDTCS[28] were also reanalysed. Finally, molecular mass estimates derived from the SAXS data were calculated by Bayesian inference of values calculated using MoW,[58] Size&Shape,[59] V$_c$,[60] and MM$_{Qp}$.[61] SAXS curves for vWF-strep-peptide at 3 mg/mL and 6 mg/mL, as well as the AD13-MDTCS-E^{225}Q: vWF-strep peptide complex, were deposited at the SASBDB repository {Kikhney, 2020 #5621} with codes SASDKT8, SASDKU8 and SASDKV8, respectively.

Ensemble generation for unbound latent AD13-MDTCS and fitting to SAXS data

The atomic coordinates of latent AD13-MDTCS (PDB 6QIG[23]; were assessed for hinge points with HingeProt,[62] and alternative conformations were generated using normal mode analysis employing an elastic network model with the ElNémo server.[63] The first five nontrivial modes were used, and the range between minimal and maximal perturbation (−500, +500) was sampled in 20 steps. These structures were supplied to GAJOE within the Ensemble Optimization Methods (EOM) program,[64,65] which is part of the ATSAS suite, to obtain a sub-ensemble that collectively best described the experimental SAXS data. GAJOE employs a genetic algorithm of artificial intelligence to minimize the discrepancy (χ^2) between the theoretical SAXS profile of the selected sub-ensemble and the experimental one according to Equation (1):

$$\chi^2 = \frac{1}{m-1} \sum_{K=1}^{m} \left(\frac{I_{exp}(q) - kI_{fit}(q)}{SE_{I_{ex\ p(q)}}} \right)^2 \tag{1}$$

where $I_{exp}(q)$ and $I_{fit}(q)$ are the experimental and ensemble-averaged scattering intensities, respectively, $SE_{I_{exp}\ (q)}$ are the associated experimental errors, and k is a scaling factor that is optimized during calculations.

vWF-strep-peptide ensemble generation

EOM was used in two steps to derive a set of conformations for vWF-strep-peptide that collectively best described the SAXS data. First, a pool of 10,000 random-coil conformations was generated for the peptide using the RanCh pool generator within the EOM program. Next, a subset of 20 conformations from this pool was selected with GAJOE based on their collective fitting to the experimental curve using Equation (1).

AD13-MDTCS-E^{225}Q:vWF-strep-peptide complex ensemble generation

A starting molecular model of active AD13-MDTCS was built for subsequent calculations. To this end, the M domain of the latent structure was remodelled with the COOT program[66] to adopt an active conformation based on active ADAMTS structures and energy-minimised with the same program. In addition, a peptide spanning L$_{1603}$–T$_{1608}$ was modelled along the active site cleft according to templates provided by other ADAMTS and MP complexes. Finally, the rest of the AD13-MDTCS structure was kept unaltered. Based on these coordinates, an initial ensemble for the complex was generated in two steps. First, various conformations of the peptidase were generated using normal mode analysis as described above for unbound latent AD13-MDTCS. Second, for each conformation of the peptidase, 1200 conformations of the peptide were generated. For these calculations, the segment of the peptide bound in the active site was fixed while the rest of the residues upstream and downstream were modelled with RanCh. This yielded a total of 120,000 structures of the complex for which the theoretical scattering profiles were computed with CRYSOL.[67] Finally, GAJOE was run for 200 cycles to select sub-ensembles of five structures from the total ensemble of complex structures. The optimized ensemble from each cycle was analysed to determine the number of structures belonging to each of the sampled normal modes of the peptidase.

Validation of SAXS ensembles with CLMS data

To analyse the agreement between the SAXS-derived structures of the complex and the restraints derived from CLMS, we first filtered the ensemble of complexes to retain only the peptidase conformations selected by EOM. Next, based on the observation that the conformational distribution of vWF-strep-peptide was not modified upon binding to the peptidase, we enlarged the ensemble complex by docking 3200 peptide conformers to the peptidase. Using this enlarged ensemble, we investigated whether the Cα atoms of the cross-linked residues were within binding distance of each other in the individual structures.

Assembling models for the AD13-MDTCS:vWF-strep-peptide complex in solution

Based on the SAXS-derived structure ensembles of the peptidase:peptide complex, we compiled sets of five molecular models that collectively best described the CLMS and H/DXMS data. To this end, we subjected the ensemble generated for analysing the agreement with CLMS to collective optimisation using CLMS and H/DXMS data. For each of the complex structures of the pool, the distance between all the cross-linked residues

measured experimentally, and the buried solvent surface area of the protected regions of AD13-MDTCS-E^{225}Q, were computed with python scripts using MDAnalysis[68] and Tcl scripts using VMD.[69] Subsequently, a genetic algorithm of artificial intelligence was developed using the DEAP library[70] to collectively fit the experimental data. Briefly, this algorithm searches for an ensemble of five conformations in which all the CLMS and H/DXMS constraints are fulfilled. The objective function maximised by the genetic algorithm is provided by Equation (2):

$$f = \frac{1}{n}\sum_{i=1}^{n}\frac{maxBS_i^{ens}}{maxBS_i^{pool}} - \frac{1}{m}\sum_{k=1}^{m}\frac{minCL_k^{ens} - minCL_k^{pool}}{maxCL_k^{pool} - minCL_k^{pool}} \quad (2)$$

where $maxBS_i$ is the maximal buried surface area found in the selected ensemble (*ens*) or in the *pool* for site i, $minCL_k$ is the minimum distance for the cross-link k for the same ensembles, and m and n are the total number of experimental cross-links and protected surface areas used for selection, respectively.

Author contributions

F.X.G.R. conceived and supervised the project; M.C.-B. and T.G. performed initial expression trials in eukaryotic systems. L.A.M. produced and purified all proteins, and performed biochemical and biophysical studies; A.S., P.P., T.G., and C.S. performed biophysical and computational studies; M.T. supervised SPR studies; J.J.E. supervised cross-linking and MS studies; P.B. supervised SAXS studies and biocomputational calculations; and F.X.G.R. and P.B. wrote the manuscript with contributions from all authors

Declaration of Competing Interest

The authors declare that they have no known competing financial interests or personal relationships that could have appeared to influence the work reported in this paper.

Appendix A. Supplementary material

Supplementary data to this article can be found online at https://doi.org/10.1016/j.jmb.2021.166954.

† Shared first authorship.

References

1. Branchford, B.R., Monahan, P.E., Di Paola, J., (2013). New developments in the treatment of pediatric hemophilia and bleeding disorders. *Curr. Opin. Pediatr.*, **25**, 23–30.
2. de Ceunynck, K., de Meyer, S.F., Vanhoorelbeke, K., (2013). Unwinding the von Willebrand factor strings puzzle. *Blood*, **121**, 270–277.
3. Denorme, F., Vanhoorelbeke, K., de Meyer, S.F., (2019). von Willebrand factor and platelet glycoprotein Ib: A thromboinflammatory axis in stroke. *Front. Immunol.*, **10**, 2884.
4. Sporn, L.A., Marder, V.J., Wagner, D.D., (1986). Inducible secretion of large, biologically potent von Willebrand factor multimers. *Cell*, **46**, 185–190.
5. Dong, J.F., Moake, J.L., Nolasco, L., Bernardo, A., Arceneaux, W., Shrimpton, C.N., et al., (2002). ADAMTS-13 rapidly cleaves newly secreted ultralarge von Willebrand factor multimers on the endothelial surface under flowing conditions. *Blood*, **100**, 4033–4039.
6. Feys, H.B., Anderson, P.J., Vanhoorelbeke, K., Majerus, E. M., Sadler, J.E., (2009). Multi-step binding of ADAMTS-13 to von Willebrand factor. *J. Thromb. Haemost.*, **7**, 2088–2095.
7. Chen, J., Fu, X., Wang, Y., Ling, M., McMullen, B., Kulman, J., et al., (2010). Oxidative modification of von Willebrand factor by neutrophil oxidants inhibits its cleavage by ADAMTS13. *Blood*, **115**, 706–712.
8. Ercig, B., Wichapong, K., Reutelingsperger, C.P.M., Vanhoorelbeke, K., Voorberg, J., Nicolaes, G.A.F., (2018). Insights into 3D structure of ADAMTS13: A stepping stone towards novel therapeutic treatment of thrombotic thrombocytopenic purpura. *Thromb. Haemost.*, **118**, 28–41.
9. Jezovnik, M.K., Poredos, P., (2010). Idiopathic venous thrombosis is related to systemic inflammatory response and to increased levels of circulating markers of endothelial dysfunction. *Int. Angiol.*, **29**, 226–231.
10. Lozano, R., Naghavi, M., Foreman, K., Lim, S., Shibuya, K., Aboyans, V., et al., (2012). Global and regional mortality from 235 causes of death for 20 age groups in 1990 and 2010: a systematic analysis for the Global Burden of Disease Study 2010. *Lancet*, **380**, 2095–2128.
11. Crawley, J.T., Scully, M.A., (2013). Thrombotic thrombocytopenic purpura: basic pathophysiology and therapeutic strategies. *Hematol. Am. Soc. Hematol. Educ. Program.*, **2013**, 292–299.
12. Maino, A., Siegerink, B., Lotta, L.A., Crawley, J.T., le Cessie, S., Leebeek, F.W., et al., (2015). Plasma ADAMTS-13 levels and the risk of myocardial infarction: an individual patient data meta-analysis. *J. Thromb. Haemost.*, **13**, 1396–1404.
13. Bansilal, S., Castellano, J.M., Fuster, V., (2015). Global burden of CVD: focus on secondary prevention of cardiovascular disease. *Int. J. Cardiol.*, **201** (Suppl 1), S1–S7.
14. Sadler, J.E., (2017). Pathophysiology of thrombotic thrombocytopenic purpura. *Blood*, **130**, 1181–1188.
15. Sadler, J.E., (2005). New concepts in von Willebrand disease. *Annu. Rev. Med.*, **56**, 173–191.
16. Branchford, B.R., Di Paola, J., (2012). Making a diagnosis of VWD. *Hematology*, **2012**, 161–167.
17. Chen, J., Hinckley, J.D., Haberichter, S., Jacobi, P., Montgomery, R., Flood, V.H., et al., (2015). Variable content of von Willebrand factor mutant monomer drives the phenotypic variability in a family with von Willebrand disease. *Blood*, **126**, 262–269.
18. Ng, C.J., di Paola, J., (2018). von Willebrand Disease: diagnostic strategies and treatment options. *Pediatr. Clin. North Am.*, **65**, 527–541.
19. Laffan, M., Sathar, J., Johnsen, J.M., (2020). von Willebrand disease: Diagnosis and treatment, treatment of women, and genomic approach to diagnosis. *Haemophilia: Off. J. World Federation Hemophilia*, **26** in press.
20. Majerus, E.M., Zheng, X., Tuley, E.A., Sadler, J.E., (2003). Cleavage of the ADAMTS13 propeptide is not required for protease activity. *J. Biol. Chem.*, **278**, 46643–46648.
21. Arolas, J.L., Goulas, T., Cuppari, A., Gomis-Rüth, F.X., (2018). Multiple architectures and mechanisms of latency in metallopeptidase zymogens. *Chem. Rev.*, **118**, 5581–5597.
22. Muia, J., Zhu, J., Greco, S.C., Vanhoorelbeke, K., Gupta, G., Westfield, L.A., et al., (2019). Phylogenetic and

functional analysis of ADAMTS13 identifies highly conserved domains essential for allosteric regulation. *Blood*, **133**, 1899–1908.

23. Petri, A., Kim, H.J., Xu, Y., de Groot, R., Li, C., Vandenbulcke, A., et al., (2019). Crystal structure and substrate-induced activation of ADAMTS13. *Nat. Commun.*, **10**, 3781.

24. Taylor, A., Vendramin, C., Oosterholt, S., Della Pasqua, O., Scully, M., (2019). Pharmacokinetics of plasma infusion in congenital thrombotic thrombocytopenic purpura. *J. Thromb. Haemost.*, **17**, 88–98.

25. Cerdà-Costa, N., Gomis-Rüth, F.X., (2014). Architecture and function of metallopeptidase catalytic domains. *Prot. Sci.*, **23**, 123–144.

26. De Ceunynck, K., Rocha, S., De Meyer, S.F., Sadler, J.E., Uji, I.H., Deckmyn, H., et al., (2014). Single particle tracking of ADAMTS13 (a disintegrin and metalloprotease with thrombospondin type-1 repeats) molecules on endothelial von Willebrand factor strings. *J. Biol. Chem.*,.

27. Takeda, S., Takeya, H., Iwanaga, S., (2012). Snake venom metalloproteinases: Structure, function and relevance to the mammalian ADAM/ADAMTS family proteins. *Biochim. Biophys. Acta, Mol. Cell. Biol. Lipids*, **1824**, 164–176.

28. Zhu, J., Muia, J., Gupta, G., Westfield, L.A., Vanhoorelbeke, K., Tolia, N.H., et al., (2019). Exploring the "minimal" structure of a functional ADAMTS13 by mutagenesis and small-angle X-ray scattering. *Blood*, **133**, 1909–1918.

29. Dent, J.A., Galbusera, M., Ruggeri, Z.M., (1991). Heterogeneity of plasma von Willebrand factor multimers resulting from proteolysis of the constituent subunit. *J. Clin. Invest.*, **88**, 774–782.

30. Zhang, Q., Zhou, Y.F., Zhang, C.Z., Zhang, X., Lu, C., Springer, T.A., (2009). Structural specializations of A2, a force-sensing domain in the ultralarge vascular protein von Willebrand factor. *Proc. Natl. Acad. Sci. USA*, **106**, 9226–9231.

31. López, J.A., Dong, J-F., (2005). Shear stress and the role of high molecular weight von Willebrand factor multimers in thrombus formation. *Blood Coagul. Fibrinolysis*, **16** (Supplementary 1), S11–S16.

32. Bortot, M., Ashworth, K., Sharifi, A., Walker, F., Crawford, N.C., Neeves, K.B., et al., (2019). Turbulent flow promotes cleavage of VWF (von Willebrand factor) by ADAMTS13 (a disintegrin and metalloproteinase with a thrombospondin type-1 motif, member 13). *Arterioscler. Thromb. Vasc. Biol.*, **39**, 1831–1842.

33. Kokame, K., Nobe, Y., Kokubo, Y., Okayama, A., Miyata, T., (2005). FRETS-VWF73, a first fluorogenic substrate for ADAMTS13 assay. *Br. J. Haematol.*, **129**, 93–100.

34. Crawley, J.T., de Groot, R., Xiang, Y., Luken, B.M., Lane, D.A., (2011). Unraveling the scissile bond: how ADAMTS13 recognizes and cleaves von Willebrand factor. *Blood*, **118**, 3212–3221.

35. de Groot, R., Bardhan, A., Ramroop, N., Lane, D.A., Crawley, J.T.B., (2009). Essential role of the disintegrin-like domain in ADAMTS13 function. *Blood*, **113**, 5609–5616.

36. Akiyama, M., Takeda, S., Kokame, K., Takagi, J., Miyata, T., (2009). Crystal structures of the noncatalytic domains of ADAMTS13 reveal multiple discontinuous exosites for von Willebrand factor. *Proc. Natl. Acad. Sci. USA*, **106**, 19274–19279.

37. Muia, J., Zhu, J., Gupta, G., Haberichter, S.L., Friedman, K.D., Feys, H.B., et al., (2014). Allosteric activation of ADAMTS13 by von Willebrand factor. *Proc. Natl. Acad. Sci. USA*, **111**, 18584–18589.

38. Anderson, P.J., Kokame, K., Sadler, J.E., (2006). Zinc and calcium ions cooperatively modulate ADAMTS13 activity. *J. Biol. Chem.*, **281**, 850–857.

39. Goulas, T., Cuppari, A., García-Castellanos, R., Snipas, S., Glockshuber, R., Arolas, J.L., et al., (2014). The pCri System: a vector collection for recombinant protein expression and purification. *PLoS ONE*, **9**, e112643

40. Marino-Puertas, L., Del Amo-Maestro, L., Taules, M., Gomis-Rüth, F.X., Goulas, T., (2019). Recombinant production of human α_2-macroglobulin variants and interaction studies with recombinant G-related α_2-macroglobulin binding protein and latent transforming growth factor-β_2. *Sci. Rep.*, **9**, 9186.

41. Mendes, S.R., Amo-Maestro, L.D., Marino-Puertas, L., Diego, I., Goulas, T., Gomis-Rüth, F.X., (2020). Analysis of the inhibiting activity of reversion-inducing cysteine-rich protein with Kazal motifs (RECK) on matrix metalloproteinases. *Sci. Rep.*, **10**, 6317.

42. Shevchenko, A., Tomas, H., Havlis, J., Olsen, J.V., Mann, M., (2006). In-gel digestion for mass spectrometric characterization of proteins and proteomes. *Nat. Protoc.*, **1**, 2856–2860.

43. Rappsilber, J., Mann, M., Ishihama, Y., (2007). Protocol for micro-purification, enrichment, pre-fractionation and storage of peptides for proteomics using StageTips. *Nat. Protoc.*, **2**, 1896–1906.

44. Götze, M., Pettelkau, J., Fritzsche, R., Ihling, C.H., Schäfer, M., Sinz, A., (2015). Automated assignment of MS/MS cleavable cross-links in protein 3D-structure analysis. *J. Am. Soc. Mass Spectrom.*, **26**, 83–97.

45. Götze, M., Pettelkau, J., Schaks, S., Bosse, K., Ihling, C.H., Krauth, F., et al., (2012). StavroX–a software for analyzing crosslinked products in protein interaction studies. *J. Am. Soc. Mass Spectrom.*, **23**, 76–87.

46. Young, M.M., Tang, N., Hempel, J.C., Oshiro, C.M., Taylor, E.W., Kuntz, I.D., et al., (2000). High throughput protein fold identification by using experimental constraints derived from intramolecular cross-links and mass spectrometry. *Proc. Natl. Acad. Sci. USA*, **97**, 5802–5806.

47. Hirose, S., Shimizu, K., Kanai, S., Kuroda, Y., Noguchi, T., (2007). POODLE-L: a two-level SVM prediction system for reliably predicting long disordered regions. *Bioinformatics*, **23**, 2046–2053.

48. Ishida, T., Kinoshita, K., (2007). PrDOS: prediction of disordered protein regions from amino acid sequence. *Nucl. Acids Res.*, **35**, W460–W464.

49. Yang, Z.R., Thomson, R., McNeil, P., Esnouf, R.M., (2005). RONN: the bio-basis function neural network technique applied to the detection of natively disordered regions in proteins. *Bioinformatics*, **21**, 3369–3376.

50. Vullo, A., Bortolami, O., Pollastri, G., Tosatto, S.C., (2006). Spritz: a server for the prediction of intrinsically disordered regions in protein sequences using kernel machines. *Nucl. Acids Res.*, **34**, W164–W168.

51. Dosztányi, Z., Csizmok, V., Tompa, P., Simon, I., (2005). IUPred: web server for the prediction of intrinsically unstructured regions of proteins based on estimated energy content. *Bioinformatics*, **21**, 3433–3434.

52. Su, C.T., Chen, C.Y., Hsu, C.M., (2007). iPDA: integrated protein disorder analyzer. *Nucl. Acids Res.*, **35**, W465–W472.

53. Kozlowski, L., Bujnicki, J.M., (2012). MetaDisorder: a meta-server for the prediction of intrinsic disorder in proteins. *BMC Bioinf.*, **13**, 111.

54. Estaña, A., Barozet, A., Mouhand, A., Vaisset, M., Zanon, C., Fauret, P., et al., (2020). Predicting secondary structure propensities in IDPs using simple statistics from three-residue fragments. *J. Mol. Biol.*, **432**, 5447–5459.

55. Franke, D., Kikhney, A.G., Svergun, D.I., (2012). Automated acquisition and analysis of small angle X-ray scattering data. *Nucl. Instrum. Methods Phys. Res. A*, **689**, 52–59.

56. Panjkovich, A., Svergun, D.I., (2018). CHROMIXS: automatic and interactive analysis of chromatography-coupled small-angle X-ray scattering data. *Bioinformatics*, **34**, 1944–1946.

57. Franke, D., Petoukhov, M.V., Konarev, P.V., Panjkovich, A., Tuukkanen, A., Mertens, H.D.T., et al., (2017). ATSAS 2.8: a comprehensive data analysis suite for small-angle scattering from macromolecular solutions. *J. Appl. Cryst.*, **50**, 1212–1225.

58. Fischer, H., de Oliveira, Neto M, Napolitano, H.B., Polikarpov, I., Craievich, A.F., (2010). Determination of the molecular weight of proteins in solution from a single small-angle X-ray scattering measurement on a relative scale. *J. Appl. Cryst.*, **43**, 101–109.

59. Franke, D., Jeffries, C.M., Svergun, D.I., (2018). Machine learning methods for X-Ray scattering data analysis from biomacromolecular solutions. *Biophys. J.*, **114**, 2485–2492.

60. Rambo, R.P., Tainer, J.A., (2013). Accurate assessment of mass, models and resolution by small-angle scattering. *Nature*, **496**, 477–481.

61. Hajizadeh, N.R., Franke, D., Jeffries, C.M., Svergun, D.I., (2018). Consensus Bayesian assessment of protein molecular mass from solution X-ray scattering data. *Sci. Rep.*, **8**, 7204.

62. Emekli, U., Schneidman-Duhovny, D., Wolfson, H.J., Nussinov, R., Haliloglu, T., (2008). HingeProt: automated prediction of hinges in protein structures. *Proteins*, **70**, 1219–1227.

63. Suhre, K., Sanejouand, Y.H., (2004). ElNémo: a normal mode web server for protein movement analysis and the generation of templates for molecular replacement. *Nucl. Acids Res.*, **32**, W610–W614.

64. Bernadó, P., Mylonas, E., Petoukhov, M.V., Blackledge, M., Svergun, D.I., (2007). Structural characterization of flexible proteins using small-angle X-ray scattering. *J. Am. Chem. Soc.*, **129**, 5656–5664.

65. Tria, G., Mertens, H.D., Kachala, M., Svergun, D.I., (2015). Advanced ensemble modelling of flexible macromolecules using X-ray solution scattering. *IUCrJ.*, **2**, 207–217.

66. Casañal, A., Lohkamp, B., Emsley, P., (2020). Current developments in *Coot* for macromolecular model building of electron cryo-microscopy and crystallographic data. *Protein Sci.*, **29**, 1069–1078.

67. Svergun, D.I., Barberato, C., Koch, M.H.J., (1995). CRYSOL – A program to evaluate X-ray solution scattering of biological macromolecules from atomic coordinates. *J. Appl. Cryst.*, **28**, 768–773.

68. Michaud-Agrawal, N., Denning, E.J., Woolf, T.B., Beckstein, O., (2011). MDAnalysis: a toolkit for the analysis of molecular dynamics simulations. *J. Comput. Chem.*, **32**, 2319–2327.

69. Humphrey, W., Dalke, A., Schulten, K., (1996). VMD: visual molecular dynamics. *J. Mol. Graph.*, **14**, 33–38.

70. Fortin, F.-A., de Rainville, F.-M., Gardner, M.-A., Parizeau, M., Gangé, C., (2012). DEAP: Evolutionary algorithms made easy. *J. Mach. Learn. Res.*, **13**, 2171–2175.

71. Gao, W., Anderson, P.J., Majerus, E.M., Tuley, E.A., Sadler, J.E., (2006). Exosite interactions contribute to tension-induced cleavage of von Willebrand factor by the antithrombotic ADAMTS13 metalloprotease. *Proc. Natl. Acad. Sci.*, **103**, 19099–19104.

72. Gao, W., Anderson, P.J., Sadler, J.E., (2008). Extensive contacts between ADAMTS13 exosites and von Willebrand factor domain A2 contribute to substrate specificity. *Blood*, **112**, 1713–1719.

73. Schelpe, A.S., Petri, A., Roose, E., Pareyn, I., Deckmyn, H., de Meyer, S.F., et al., (2020). Antibodies that conformationally activate ADAMTS13 allosterically enhance metalloprotease domain function. *Blood Adv.*, **4**, 1072–1080.

74. Pos, W., Crawley, J.T.B., Fijnheer, R., Voorberg, J., Lane, D.A., Luken, B.M., (2010). An autoantibody epitope comprising residues R660, Y661, and Y665 in the ADAMTS13 spacer domain identifies a binding site for the A2 domain of VWF. *Blood*, **115**, 1640–1649.

75. de Groot, R., Lane, D.A., Crawley, J.T.B., (2015). The role of the ADAMTS13 cysteine-rich domain in VWF binding and proteolysis. *Blood*, **125**, 1968–1975.

76. Bernado, P., Blackledge, M., (2009). A self-consistent description of the conformational behavior of chemically denatured proteins from NMR and small angle scattering. *Biophys. J.*, **97**, 2839–2845.

77. Riback, J.A., Bowman, M.A., Zmyslowski, A.M., Knoverek, C.R., Jumper, J.M., Hinshaw, J.R., et al., (2017). Innovative scattering analysis shows that hydrophobic disordered proteins are expanded in water. *Science*, **358**, 238–241.

78. Fuxreiter, M., (2012). Fuzziness: linking regulation to protein dynamics. *Mol. BioSyst.*, **8**, 168–177.

79. Sharma, R., Raduly, Z., Miskei, M., Fuxreiter, M., (2015). Fuzzy complexes: specific binding without complete folding. *FEBS Lett.*, **589**, 2533–2542.

80. Cordeiro, T.N., Sibille, N., Germain, P., Barthe, P., Boulahtouf, A., Allemand, F., et al., (2019). Interplay of protein disorder in retinoic acid receptor heterodimer and its corepressor regulates gene expression. *Structure*, **27**, 1270–1285.